# High-Order $k$-Exact Finite Volume Scheme for Vertex-Centered Unstructured Grids

Florian Setzwein* and Peter Ess†

Institute of Combustion Technology, German Aerospace Center (DLR), Stuttgart, 70569, Germany

Peter Gerlinger‡

IVLR, University of Stuttgart, Stuttgart, 70569, Germany

**We present a spatially third-order accurate unstructured finite volume scheme, which is based on the multiple-correction hybrid $k$-exact scheme. A recursive correction of Green-Gauss derivatives is used to reconstruct a $k$-exact polynomial within each cell, while only involving communication between direct cell neighbors. The scheme is extended to a $k$-exact reconstruction on vertex-centered median dual grids and utilized for the discretization of the incompressible Euler equations, showing its applicability for the solution of Poisson's equation. The spatial accuracy is demonstrated on various, highly deformed unstructured grids and for various benchmark tests. It is shown that the scheme can clearly enhance the accuracy of time-dependent incompressible flow solutions.**

## I. Introduction

High-order methods have the potential of reducing computational effort through enhanced resolution properties and a larger decrease of truncation errors in comparison to conventional discretization schemes. This offers advantages in particular for Large-Eddy Simulations of complex flows to meet the high-resoltion requirements for reasonably coarse grids.[1] A possibility to achieve a high-order accuracy is the $k$-exact finite volume approach, for which the solution is locally reconstructed by means of polynomials within each control volume.[2] This is realized by relating successive derivatives of the solution to the polynomial coefficients, which are generally calculated with least-squares approximations of volume-averaged quantities in the vicinity of a cell.[3] Haider et al.[4–6] presented a general procedure for the $k$-exact reconstruction on unstructured grids, based on recursive corrections of the approximate successive derivatives, which requires only exchange between adjacent cells. Pont et al.[3] adopted this approach where required derivatives were calculated with a Green-Gauss formulation, ensuring consistency on highly deformed grids. Within this work, the multiple-correction hybrid $k$-exact scheme by Pont et al. is extended for a vertex-centered median dual tesselation of arbitrary grids, which offers a higher number of direct neighbors for each cell and therefore leads to a higher accuracy for the polynomial reconstruction. The scheme is applied to the incompressible Euler equations, but can be extended for the full incompressible and compressible Navier-Stokes equations with only minor modifications. The improved spatial accuracy is demonstrated by the calculation of a scalar gradient, where it is shown that first derivatives can be approximated with an accuracy of second order in space even on strongly distorted, unstructured grids. Furthermore, the enhanced spatial accuracy is demonstrated for the linear convection of a scalar quantity, as well as the nonlinear transport of a vortex in a uniform flow field. It is shown that the proposed scheme leads to a significant reduction of computational elements needed to obtain a prescribed quality of the solution when compared to a conventional discretization scheme.

*PhD Student, German Aerospace Center (DLR), Stuttgart, 70569, Germany
†Postdoctoral Fellow, Senior AIAA Member, German Aerospace Center (DLR), Stuttgart, 70569, Germany
‡Professor, IVLR University of Stuttgart, Stuttgart, 70569, Germany

## II. Multiple-Correction Approach for Vertex-Centered Grids

We restrict ourselves to the discretization of the divergence form of the convective operator

$$\frac{\partial \phi}{\partial t} + \nabla \cdot (\mathbf{u}\phi) = S, \tag{1}$$

describing the convection of a physical quantity $\phi(\mathbf{x}, t)$ in an incompressible flowfield with velocity $\mathbf{u}(\mathbf{x}, t)$ under the influence of a source $S(\mathbf{x}, t)$. The convective transport is investigated in a domain $\Omega \subset \mathbb{R}^d$, which is discretized by a tesselation of tetrahedral, hexagonal, prismatic and pyramidal elements for $d = 3$ or triangular and quadrilateral elements for $d = 2$, referred to as the primary grid $\mathcal{P}(\Omega)$. A vertex-centered formulation of the primary grid is obtained by constructing polyhedral elements from the centroids of adjacent elements, faces and edges around each primary grid node. The resulting set of $N$ non-overlapping complex polyhedral cells, which are compounds of triangular faces, are referred to as the median dual grid tesselation $\mathcal{D}(\Omega)$. Two elements $\Omega_\alpha$ and $\Omega_\beta$ are considered to be adjacent if they share a commong face $A_{\alpha\beta}$. All adjacent elements of a cell $\Omega_\alpha$ are referred to as its $1^{st}$ neighborhood, signed as $\mathbb{V}_\alpha^{(1)}$. The $n^{th}$ neighborhood of $\Omega_\alpha$ is defined recursively via the neighborhoods of its adjacent elements $\mathbb{V}_\alpha^{(n)} := \bigcup_{\gamma \in \mathbb{V}_\alpha^{(n-1)}} \mathbb{V}_\gamma^{(1)}$. Figure 1 shows a primary grid $\mathcal{P}(\Omega)$, its respective median dual tesselation $\mathcal{D}(\Omega)$ and the first and second neighborhood of a median dual cell $\Omega_\alpha$ for $d = 2$.

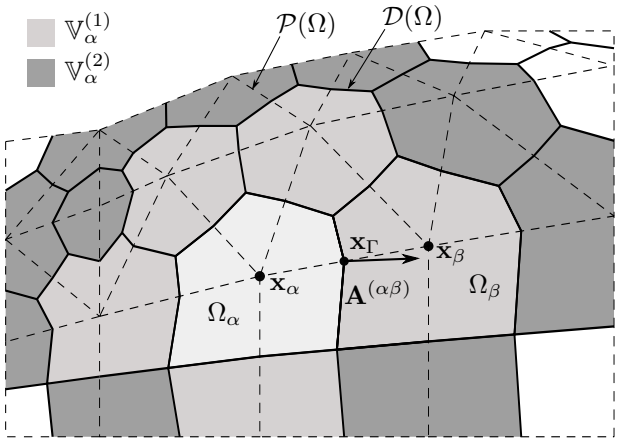


Figure 1: Median dual grid in 2D, indicated in solid lines. The corresponding primary grid is drawn in dashed lines. The simulation variables are stored at the location of primary grid nodes, e.g. $\mathbf{x}_\alpha$ or $\mathbf{x}_\beta$.

The volume-average $\overline{\psi}_\alpha$ of any quantity within a control volume $\Omega_\alpha$ is defined by

$$\overline{\psi}_\alpha := \frac{1}{|\Omega_\alpha|} \iiint_{\Omega_\alpha} \psi(\mathbf{x}) \, \mathrm{d}V. \tag{2}$$

In the scope of a finite volume approach, equation (1) is volume-integrated over all control volumes in $\mathcal{D}(\Omega)$. This leads to a system of $N$ equations with unknown volume-averages $\overline{\phi}_\alpha$ acting as degrees of freedom:

$$\frac{\partial \overline{\phi}_\alpha}{\partial t} + \frac{1}{|\Omega_\alpha|} \sum_{\beta \in \mathbb{V}_\alpha^{(1)}} \iint_{A_{\alpha\beta}} (\mathbf{u}\phi) \cdot \mathbf{n} \, \mathrm{d}A = \overline{S}. \tag{3}$$

The surface integrals, referred to as fluxes, arise due to the application of the Gauss theorem and must be approximated for every median dual cell face $A_{\alpha\beta}$. As starting point, the function $(\mathbf{u}\phi)$ is reconstructed through a Taylor series of degree 2, in order to preserve a 2-exact reonstruction. It is expanded around a point $\mathbf{x}_\Gamma$ on face $A_{\alpha\beta}$ and integrated over the surface of $A_{\alpha\beta}$

$$\iint_{A_{\alpha\beta}} (\mathbf{u}\phi) \cdot \mathbf{n} \, \mathrm{d}A = (u_i\phi)_\Gamma \mathcal{S}_i^{(\alpha\beta)} + \left.\frac{\partial (u_j\phi)}{\partial x_k}\right|_{\mathbf{x}_\Gamma} \mathcal{S}_{j,k}^{(\alpha\beta)} + \frac{1}{2} \left.\frac{\partial^2 (u_l\phi)}{\partial x_m \partial x_n}\right|_{\mathbf{x}_\Gamma} \mathcal{S}_{l,mn}^{(\alpha\beta)} + \mathcal{O}(h^3), \tag{4}$$

with $h$ being a characteristic cell width of the median dual mesh. The surface-integrated Taylor-series expansion contains terms, that are referred to as rank $p$ geometric surface tensors $\boldsymbol{\mathcal{S}}^{(\alpha\beta)}$, defined by

$$\mathcal{S}^{(\alpha\beta)}_{i,j_1 j_2 \dots j_p} := \iint_{A_{\alpha\beta}} n_i \left(x_{j_1} - x_{j_1,\Gamma}\right)\left(x_{j_2} - x_{j_2,\Gamma}\right) \dots \left(x_{j_p} - x_{j_p,\Gamma}\right) \mathrm{d}A. \tag{5}$$

The subscripts $i$ and $j_p$ are separated by a comma, in order to highlight that $i$ indicates the face normal direction and $j_p$ the spatial direction of the distance terms $\left(x_{j_p} - x_{j_p,\Gamma}\right)$. The superscript in brackets specifies the adjacent elements $\Omega_\alpha$ and $\Omega_\beta$ of the face on which point $\mathbf{x}_\Gamma$ for the Taylor series expansion is located. The rank 0 geometric surface tensor $\mathcal{S}^{(\alpha\beta)}_i$ denotes the joint normal of all sub-faces of a median dual cell face $A_{\alpha\beta}$. All surface tensors depend solely on the geometry of the median-dual grid and can be computed in a preprocessing step prior to the simulation. For a 2-exact reconstruction, the primitive field variables $\phi$ and $\mathbf{u}$ are approximated as polynomial functions of order $k = 2$ in the vicinity of an element $\Omega_\alpha$:

$$u_i(\mathbf{x}) = u_{i,\alpha} + \left.\frac{\partial u_i}{\partial x_j}\right|_{\mathbf{x}_\alpha} \left(x_j - x_{j,\alpha}\right) + \frac{1}{2} \left.\frac{\partial^2 u_i}{\partial x_k \partial x_l}\right|_{\mathbf{x}_\alpha} \left(x_k - x_{k,\alpha}\right)\left(x_l - x_{l,\alpha}\right) + \mathcal{O}(h^3), \tag{6}$$

$$\phi(\mathbf{x}) = \phi_\alpha + \left.\frac{\partial \phi}{\partial x_j}\right|_{\mathbf{x}_\alpha} \left(x_j - x_{j,\alpha}\right) + \frac{1}{2} \left.\frac{\partial^2 \phi}{\partial x_k \partial x_l}\right|_{\mathbf{x}_\alpha} \left(x_k - x_{k,\alpha}\right)\left(x_l - x_{l,\alpha}\right) + \mathcal{O}(h^3). \tag{7}$$

The point of evaluation $\mathbf{x}_\alpha$ referes to the primary grid node position, around which a median dual cell $\Omega_\alpha$ is constructed. For the approximation of the flux integral, equations (6) and (7) are inserted into equation (4). Applying the chain rule, the fluxes can be expressed as:

$$\iint_{A_{\alpha\beta}} (\mathbf{u}\phi) \cdot \mathbf{n} \, \mathrm{d}A = \dot{m}_\Gamma \phi_\Gamma + \dot{m}_{j,\Gamma} \left.\frac{\partial \phi}{\partial x_j}\right|_{\mathbf{x}_\Gamma} + \frac{1}{2} \dot{m}_{kl,\Gamma} \left.\frac{\partial^2 \phi}{\partial x_k \partial x_l}\right|_{\mathbf{x}_\Gamma} + \mathcal{O}(h^3). \tag{8}$$

The terms $\dot{m}_\Gamma$, $\dot{m}_{j,\Gamma}$ and $\dot{m}_{kl,\Gamma}$, referred to as rank 0 to rank 2 massflux tensors of a face $A_{\alpha\beta}$, are defined by

$$\dot{m}_\Gamma := u_{i,\Gamma} \mathcal{S}^{(\alpha\beta)}_i + \left.\frac{\partial u_j}{\partial x_k}\right|_{\mathbf{x}_\Gamma} \mathcal{S}^{(\alpha\beta)}_{j,k} + \frac{1}{2} \left.\frac{\partial^2 u_l}{\partial x_m \partial x_n}\right|_{\mathbf{x}_\Gamma} \mathcal{S}^{(\alpha\beta)}_{l,mn}, \tag{9a}$$

$$\dot{m}_{j,\Gamma} := u_{i,\Gamma} \mathcal{S}^{(\alpha\beta)}_{i,j} + \left.\frac{\partial u_k}{\partial x_l}\right|_{\mathbf{x}_\Gamma} \mathcal{S}^{(\alpha\beta)}_{k,jl}, \tag{9b}$$

$$\dot{m}_{jk,\Gamma} := u_{i,\Gamma} \mathcal{S}^{(\alpha\beta)}_{i,jk}. \tag{9c}$$

It is worth mentioning, that $u_{i,\alpha}$ and $\phi_\alpha$, as well as their derivatives, represent point values at location $\mathbf{x}_\alpha$. These values are reconstructed from respective volume-averages $\overline{u_i}$ and $\overline{\phi}$ of neighboring elements in the vicinity of a cell $\Omega_\alpha$, in order to solve the system of equations. To obtain a third order accuracy in space, the values $u_{i,\alpha}$ and $\phi_\alpha$ must be approximated with a numerical error of $\mathcal{O}(h^3)$, their first derivatives with $\mathcal{O}(h^2)$ and their second derivatives with $\mathcal{O}(h)$. The reconstruction of point values $u_{i,\alpha}$ and $\phi_\alpha$ is maintained by volume-integrating equations (6) and (7), which will be explained later on. The prescribed accuracy of derivatives is preserved through the multiple-correction approach, by relating the polynomial coefficients to approximate derivatives, which in turn are derived from volume-averages within the neighborhood of $\Omega_\alpha$. The degree $k$ of the polynomial is increased recursively with successive corrections of these approximated derivatives to higher orders of accuracy. This is realized via information from more and more neighborhoods of $\Omega_\alpha$. Finally, the point values at primary grid node positions are used to calculate face-values $u_{i,\Gamma}$ and $\phi_\Gamma$ through equations (6) and (7), which are then used to approximate the flux integral with equation (8).

### A. 1-Exact Gradient Approximation

The successive correction of approximate derivatives is shown for the transported scalar $\phi$ and applies similarly to $u_i$. First, the solution in the vicinity of $\Omega_\alpha$ is reconstructed through a 1-exact function

$$\phi(\mathbf{x}) = \phi_\alpha + \left.\frac{\partial \phi}{\partial x_j}\right|_{\mathbf{x}_\alpha} \left(x_j - x_{j,\alpha}\right) + \mathcal{O}(h^2). \tag{10}$$

The first derivative is approximated using a Green-Gauss gradient operator, denoted by squared brackets, which yields an error of $\mathcal{O}(1)$ on deformed meshes

$$\frac{\partial}{\partial x_j}\left[\,\overline{\phi}\,\right]_\alpha := \frac{1}{|\Omega_\alpha|}\sum_{\beta\in\mathbb{V}_\alpha^{(1)}}\left[w_{\alpha\beta}\overline{\phi}_\beta + (1-w_{\alpha\beta})\overline{\phi}_\alpha\right]\mathcal{S}_j^{(\alpha\beta)}. \tag{11}$$

The weights $w_{\alpha\beta}$ are calculated according to

$$w_{\alpha\beta} = \frac{||\mathbf{x}_\Gamma - \mathbf{x}_\beta||}{||\mathbf{x}_\alpha - \mathbf{x}_\beta||}, \tag{12}$$

and reduce to a value of 1/2, if $\mathbf{x}_\Gamma$ is chosen to be the bisecting point of a primary grid edge between points $\mathbf{x}_\alpha$ and $\mathbf{x}_\beta$. A 1-exact gradient formulation is obtained with a correction matrix $\mathbf{G}_\alpha$, which ensures gradients with accuracy $\mathcal{O}(h)$ on arbitrary grids. This is referred to as the recursive correction approach, that has been introduced by Pont et al.[3] for cell-centered grids. In order to derive the correction matrix for vertex-centered grids, the 1-exact reconstruction function (10) is volume-averaged on all neighboring cells $\Omega_\beta$ according to equation (2). This leads to an expression for $\overline{\phi}_\beta$ in terms of $\overline{\phi}_\alpha$.

$$\overline{\phi}_\beta = \phi_\alpha + \left.\frac{\partial\phi}{\partial x_i}\right|_{\mathbf{x}_\alpha}\mathcal{M}_i^{(\beta,\alpha)} + \mathcal{O}(h^2) = \overline{\phi}_\alpha + \left.\frac{\partial\phi}{\partial x_i}\right|_{\mathbf{x}_\alpha}\left(\mathcal{M}_i^{(\beta,\alpha)} - \mathcal{M}_i^{(\alpha,\alpha)}\right) + \mathcal{O}(h^2) \tag{13}$$

with

$$\overline{\phi}_\alpha = \phi_\alpha + \left.\frac{\partial\phi}{\partial x_i}\right|_{\mathbf{x}_\alpha}\mathcal{M}_i^{(\alpha,\alpha)} + \mathcal{O}(h^2). \tag{14}$$

The volume-integration leads to metrics which are referred to as rank $p$ geometric volume moment tensors

$$\mathcal{M}_{i_1 i_2 \ldots i_p}^{(\beta,\alpha)} = \frac{1}{|\Omega_\beta|}\iiint_{\Omega_\beta}(x_{i_1} - x_{i_1,\alpha})(x_{i_2} - x_{i_2,\alpha})\ldots\left(x_{i_p} - x_{i_p,\alpha}\right)\mathrm{d}V. \tag{15}$$

It should be noted, that the first superscript $\beta$ denotes the volume $\Omega_\beta$ for performing the averaging and the second superscript $\alpha$ denotes the point $\mathbf{x}_\alpha$ used for centering the moment. Similar to the surface moments, the volume moments depend on the median-dual grid and are calculated analytically prior to the simulation. Only moment tensors $\mathcal{M}_{i_1 i_2 \ldots i_p}^{(\alpha,\alpha)}$ must be stored for each element, since the expression $\mathcal{M}_{i_1 i_2 \ldots i_p}^{(\beta,\alpha)}$ between two adjacent cells $\alpha$ and $\beta$ can be deduced from binomial expansion (see Charest et al.[7] and Ollivier-Gooch and Van Altena[8] for reference). Further information concerning the calculation of geometric tensors can be found in the work of Pozo et al.[9] For general cell-centered finite volume approaches, grid elements consist of simple polyhedra, such as tetrahedrals or quadrilaterals, and the flow data is stored at the respective element centroids. As a result, the rank 1 geometric volume moments for such elements equal to zero. This condition was exploited in the cell-centered multiple-correction approach by Pont et al.[3] for the calculation of 1- and 2-exact gradients on deformed grids. In contrast, vertex-centered grids exhibit much more complex element forms, since single cells are connected to more neighbors. If the flow data is stored at a primary grid vertex location $\mathbf{x}_\alpha$, which does not coincide in general with the centroid of a median dual element, the condition $\mathcal{M}_i^{(\alpha,\alpha)} = 0$ is violated. Thus, the aim of this paper is to extend the multiple-correction method so that it can also be applied to arbitrary elements occuring in vertex-centered grids. Starting point is the substitution of equation (13) into (11). After a rearrangement of terms, the 0-exact Green-Gauss gradient operator can be written by means of a linear mapping of the 1-exact first derivative of $\phi$ via a matrix $\mathbf{G}_\alpha$, referred to as gradient correction matrix:

$$\frac{\partial}{\partial x_i}\left[\,\overline{\phi}\,\right]_\alpha = G_{ij,\alpha}\left.\frac{\partial\phi}{\partial x_j}\right|_{\mathbf{x}_\alpha} + \mathcal{O}(h). \tag{16}$$

This correction matrix can be calculated through

$$G_{ij,\alpha} = \frac{\partial}{\partial x_i}\left[\,\mathcal{M}_j\,\right]_\alpha, \tag{17}$$

with the gradient of the first geometric volume moments of $\Omega_\alpha$ being defined according to

$$\frac{\partial}{\partial x_i}\left[\,\mathcal{M}_j\,\right]_\alpha := \frac{1}{|\Omega_\alpha|}\sum_{\beta\in\mathbb{V}_\alpha^{(1)}}\left[w_{\alpha\beta}\mathcal{M}_j^{(\beta,\alpha)} + (1-w_{\alpha\beta})\mathcal{M}_j^{(\alpha,\alpha)}\right]\mathcal{S}_i^{(\alpha\beta)}. \tag{18}$$

This expression is simply a Green-Gauss gradient operation applied to the respective geometric moment tensor entries. Notice that the centering of the geometric volume moments in equation (18) varies according to the respective element $\Omega_\alpha$. Finally a 1-exact gradient operator at the cell centroid $\mathbf{x}_\alpha$ is defined by inverting the correction matrix $\mathbf{G}_\alpha$ and is indicated with an asterisk

$$\frac{\partial}{\partial x_i}\big[\,\overline{\phi}\,\big]^*_\alpha := G^{-1}_{ij,\alpha}\frac{\partial}{\partial x_j}\big[\,\overline{\phi}\,\big]_\alpha. \tag{19}$$

### B. 1-Exact Hessian-Matrix Approximation

The second derivative of $\phi(\mathbf{x})$ is approximated by applying the Green-Gauss gradient operator on the 1-exact gradient of the field variable $\phi$. This leads to the approximated Hessian matrix operator $\frac{\partial^2}{\partial x_i \partial x_j}[\,\phi\,]_\alpha$ with an accuracy of $\mathcal{O}(1)$ on deformed meshes

$$\frac{\partial^2}{\partial x_i \partial x_j}\big[\,\overline{\phi}\,\big]_\alpha := \frac{\partial}{\partial x_i}\left[\,\frac{\partial}{\partial x_j}\big[\,\overline{\phi}\,\big]^*\,\right]_\alpha = \frac{1}{|\Omega_\alpha|}\sum_{\beta\in\mathbb{V}^{(1)}_\alpha}\left[w_{\alpha\beta}\frac{\partial}{\partial x_j}[\,\phi\,]^*_\beta + (1-w_{\alpha\beta})\,\frac{\partial}{\partial x_j}[\,\phi\,]^*_\alpha\right]\mathcal{S}_i^{(\alpha\beta)}. \tag{20}$$

Similar to the correction matrix of the 1-exact gradient operator, there exists a relation between the 2-exact second derivatives $\frac{\partial^2\phi}{\partial x_i\partial x_j}\Big|_{\mathbf{x}_\alpha}$ and the 0-exact Hessian operator $\frac{\partial^2}{\partial x_i\partial x_j}\big[\,\overline{\phi}\,\big]_\alpha$, which reads

$$\begin{aligned}\frac{\partial^2}{\partial x_i\partial x_j}\big[\,\overline{\phi}\,\big]_\alpha + \frac{\partial^2}{\partial x_j\partial x_i}\big[\,\overline{\phi}\,\big]_\alpha = {}& \delta_{ik}\,\frac{\partial^2\phi}{\partial x_j\partial x_k}\bigg|_{\mathbf{x}_\alpha} + \frac{1}{2}\frac{\partial^2}{\partial x_i\partial x_j}[\,\mathcal{M}_{mn}\,]_\alpha\,\frac{\partial^2\phi}{\partial x_m\partial x_n}\bigg|_{\mathbf{x}_\alpha}\\ &+ \delta_{jl}\,\frac{\partial^2\phi}{\partial x_i\partial x_l}\bigg|_{\mathbf{x}_\alpha} + \frac{1}{2}\frac{\partial^2}{\partial x_j\partial x_i}[\,\mathcal{M}_{pq}\,]_\alpha\,\frac{\partial^2\phi}{\partial x_p\partial x_q}\bigg|_{\mathbf{x}_\alpha}\\ &+ \mathcal{O}(h),\end{aligned} \tag{21}$$

with the unit matrix $\delta_{ij}$. The derivation of equation (21) is based on the work of Haider et al.[4] and Pont et al.[3] and has been adjusted in this work to allow the calculation for vertex-centered grids. The full derivation is shown in appendix A. Relation (21) can be transformed into a linear mapping between the tensors $\frac{\partial^2\phi}{\partial x_i\partial x_j}\Big|_{\mathbf{x}_\alpha}$ and $\frac{\partial^2}{\partial x_i\partial x_j}\big[\,\overline{\phi}\,\big]_\alpha$ through a correction matrix $\mathbf{H}_\alpha$. For this purpose the symmetric rank 2 tensors are vectorized, as for example the Hessian matrix and the geometric volume tensor. Such vectorized tensors will be denoted by a circumflex and their entries are arranged in the same order. For example, the vectorized Hessian matrix $\frac{\partial^2\phi}{\partial x_i\partial x_j}\Big|_{\mathbf{x}_\alpha}$ reads

$$\widehat{\mathbf{D}}^{(2)}\phi\Big|_{\mathbf{x}_\alpha} = \Big(\,\frac{\partial^2\phi}{\partial x_1\partial x_1}\Big|_{\mathbf{x}_\alpha}\quad \frac{\partial^2\phi}{\partial x_1\partial x_2}\Big|_{\mathbf{x}_\alpha}\quad \frac{\partial^2\phi}{\partial x_1\partial x_3}\Big|_{\mathbf{x}_\alpha}\quad \frac{\partial^2\phi}{\partial x_2\partial x_2}\Big|_{\mathbf{x}_\alpha}\quad \frac{\partial^2\phi}{\partial x_2\partial x_3}\Big|_{\mathbf{x}_\alpha}\quad \frac{\partial^2\phi}{\partial x_3\partial x_3}\Big|_{\mathbf{x}_\alpha}\,\Big)^T. \tag{22}$$

Now relationship (21) can be represented by a linear mapping between the vectorized 0-exact Hessian matrix operator $\widehat{D}^{(2)}_i\big[\,\overline{\phi}\,\big]_\alpha$ and the vectorized second derivatives $\widehat{D}^{(2)}_j\phi\Big|_{\mathbf{x}_\alpha}$

$$\widehat{D}^{(2)}_i\big[\,\overline{\phi}\,\big]_\alpha = H_{ij,\alpha}\;\widehat{D}^{(2)}_j\phi\Big|_{\mathbf{x}_\alpha} + \mathcal{O}(h), \tag{23}$$

with the correction matrix $\mathbf{H}_\alpha$ defined as

$$\mathbf{H}_\alpha = \begin{bmatrix} 1+\frac{\partial^2}{\partial x_1\partial x_1}[\,\mathcal{M}_{11}\,]_\alpha & 2\,\frac{\partial^2}{\partial x_1\partial x_1}[\,\mathcal{M}_{12}\,]_\alpha & 2\,\frac{\partial^2}{\partial x_1\partial x_1}[\,\mathcal{M}_{13}\,]_\alpha & \dots & \frac{\partial^2}{\partial x_1\partial x_1}[\,\mathcal{M}_{33}\,]_\alpha\\ \frac{\partial^2}{\partial x_1\partial x_2}[\,\mathcal{M}_{11}\,]_\alpha & 1+2\,\frac{\partial^2}{\partial x_1\partial x_2}[\,\mathcal{M}_{12}\,]_\alpha & 2\,\frac{\partial^2}{\partial x_1\partial x_2}[\,\mathcal{M}_{13}\,]_\alpha & \dots & \frac{\partial^2}{\partial x_1\partial x_2}[\,\mathcal{M}_{33}\,]_\alpha\\ \vdots & \vdots & \vdots & \dots & \vdots\\ \frac{\partial^2}{\partial x_3\partial x_3}[\,\mathcal{M}_{11}\,]_\alpha & 2\,\frac{\partial^2}{\partial x_3\partial x_3}[\,\mathcal{M}_{12}\,]_\alpha & 2\,\frac{\partial^2}{\partial x_3\partial x_3}[\,\mathcal{M}_{13}\,]_\alpha & \dots & 1+\frac{\partial^2}{\partial x_3\partial x_3}[\,\mathcal{M}_{33}\,]_\alpha \end{bmatrix}. \tag{24}$$

The expression $\frac{\partial^2}{\partial x_i\partial x_j}[\,\mathcal{M}_{kl}\,]_\alpha$ denotes the 0-exact Hessian matrix operator of equation (20) applied on the rank 2 volume moment tensor. Finally, the 1-exact Hessian matrix operator is introduced analogously to the 1-exact gradient operator:

$$\widehat{D}^{(2)}_i\big[\,\overline{\phi}\,\big]^*_\alpha := H^{-1}_{ij,\alpha}\;\widehat{D}^{(2)}_j\big[\,\overline{\phi}\,\big]_\alpha. \tag{25}$$

### C. 2-Exact Gradient Approximation

A 2-exact gradient operator, which introduces an error of $\mathcal{O}(h^2)$, is derived by expressing $\overline{\phi}_\beta$ by means of $\overline{\phi}_\alpha$ in an approach similar to that in equation (13), but for the 2-exact reconstruction function (7). Inserting this expression for $\overline{\phi}_\beta$ into the 1-exact gradient operator (19) leads to the relation

$$\frac{\partial}{\partial x_i}\left[\,\overline{\phi}\,\right]^*_\alpha = \underbrace{\frac{\partial}{\partial x_i}\left[\,\mathcal{M}_k\,\right]^*_\alpha}_{=\delta_{ik}} \left.\frac{\partial \phi}{\partial x_k}\right|_{\mathbf{x}_\alpha} + \frac{1}{2}\frac{\partial}{\partial x_i}\left[\,\mathcal{M}_{lm}\,\right]^*_\alpha \left.\frac{\partial^2 \phi}{\partial x_l \partial x_m}\right|_{\mathbf{x}_\alpha} + \mathcal{O}(h^2). \tag{26}$$

It can be shown, that the 1-exact gradient expression of the first geometric volume moments equals the identity matrix. For the tensor $\frac{\partial}{\partial x_i}\left[\,\mathcal{M}_{lm}\,\right]^*_\alpha$, the 1-exact gradient operator of equation (19) is applied on the rank 2 geometric volume moment tensor. The second derivatives $\left.\frac{\partial^2 \phi}{\partial x_l \partial x_m}\right|_{\mathbf{x}_\alpha}$ in equation (26) are substituted by their 1-exact Hessian matrix operator counterparts $\frac{\partial^2}{\partial x_l \partial x_m}\left[\,\overline{\phi}\,\right]^*_\alpha$. This symmetric rank 2 tensor is also vectorized to finally obtain the following form of the 2-exact gradient operator

$$\frac{\partial}{\partial x_i}\left[\,\overline{\phi}\,\right]^{**}_\alpha := \frac{\partial}{\partial x_i}\left[\,\overline{\phi}\,\right]^*_\alpha - \frac{1}{2} G^*_{ij,\alpha} \widehat{D}^{(2)}_j \left[\,\overline{\phi}\,\right]^*_\alpha. \tag{27}$$

The $(3 \times 6)$ matrix $G^*_{ij,\alpha}$ results from the vectorization and can be calculated according to

$$\mathbf{G}^*_\alpha = \begin{bmatrix} \frac{\partial}{\partial x_1}\left[\,\mathcal{M}_{11}\,\right]^*_\alpha & 2\,\frac{\partial}{\partial x_1}\left[\,\mathcal{M}_{12}\,\right]^*_\alpha & 2\,\frac{\partial}{\partial x_1}\left[\,\mathcal{M}_{13}\,\right]^*_\alpha & \dots & \frac{\partial}{\partial x_1}\left[\,\mathcal{M}_{33}\,\right]^*_\alpha \\ \frac{\partial}{\partial x_2}\left[\,\mathcal{M}_{11}\,\right]^*_\alpha & 2\,\frac{\partial}{\partial x_2}\left[\,\mathcal{M}_{12}\,\right]^*_\alpha & 2\,\frac{\partial}{\partial x_2}\left[\,\mathcal{M}_{13}\,\right]^*_\alpha & \dots & \frac{\partial}{\partial x_2}\left[\,\mathcal{M}_{33}\,\right]^*_\alpha \\ \frac{\partial}{\partial x_3}\left[\,\mathcal{M}_{11}\,\right]^*_\alpha & 2\,\frac{\partial}{\partial x_3}\left[\,\mathcal{M}_{12}\,\right]^*_\alpha & 2\,\frac{\partial}{\partial x_3}\left[\,\mathcal{M}_{13}\,\right]^*_\alpha & \dots & \frac{\partial}{\partial x_3}\left[\,\mathcal{M}_{33}\,\right]^*_\alpha \end{bmatrix}. \tag{28}$$

### D. Calculation of Face-Fluxes

Given the 2-exact derivatives and the volume-average $\overline{\phi}$, it is now possible to approximate point values of $\phi(\mathbf{x})$ within a cell $\Omega_\alpha$ by volume-integration of equation (7) and substitution of derivatives with respective gradient and Hessian operators.

$$\phi_\alpha = \overline{\phi}_\alpha - \frac{\partial}{\partial x_i}\left[\,\overline{\phi}\,\right]^{**}_\alpha \mathcal{M}^{(\alpha,\alpha)}_i - \frac{1}{2}\frac{\partial^2}{\partial x_j \partial x_k}\left[\,\overline{\phi}\,\right]^*_\alpha \mathcal{M}^{(\alpha,\alpha)}_{jk} + \mathcal{O}(h^3) \tag{29}$$

Point values at faces are finally reconstructed by

$$\phi_\Gamma = \phi_\alpha + \frac{\partial}{\partial x_i}\left[\,\overline{\phi}\,\right]^{**}_\alpha (x_{\Gamma,i} - x_{\alpha,i}) + \frac{1}{2}\frac{\partial^2}{\partial x_j \partial x_k}\left[\,\overline{\phi}\,\right]^*_\alpha (x_{\Gamma,j} - x_{\alpha,j})\,(x_{\Gamma,k} - x_{\alpha,k}) + \mathcal{O}(h^3), \tag{30}$$

$$\left.\frac{\partial \phi}{\partial x_i}\right|_{\mathbf{x}_\Gamma} = \frac{\partial}{\partial x_i}\left[\,\overline{\phi}\,\right]^{**}_\alpha + \frac{\partial^2}{\partial x_i \partial x_j}\left[\,\overline{\phi}\,\right]^*_\alpha (x_{j,\Gamma} - x_{j,\alpha}) + \mathcal{O}(h^2), \tag{31}$$

$$\left.\frac{\partial^2 \phi}{\partial x_i \partial x_j}\right|_{\mathbf{x}_\Gamma} = \frac{\partial^2}{\partial x_i \partial x_j}\left[\,\overline{\phi}\,\right]^*_\alpha + \mathcal{O}(h). \tag{32}$$

The same procedure applies to the velocities $u_i(\mathbf{x})$. The fluxes of equation (4) are evaluated for both adjacent cells $\Omega_\alpha$ and $\Omega_\beta$ and the resulting values can be used as input for an approximate Riemann solver. In this work a Riemann-free approach is employed, considering only smooth continuous solutions. The fluxes are calculated according to a hybrid scheme by Pont et al.[3]

$$\phi_\Gamma = \frac{1+\Theta}{2}\phi_{\Gamma,U} + \frac{1-\Theta}{2}\phi_{\Gamma,D}, \tag{33}$$

with subscripts $U$ and $D$ denoting upwind and downwind locations of the respective neighboring cells. The same weighting approach between upwind and downwind locations is utilized for the derivatives. The scheme lowers numerical dissipation in vortex-dominated regions using a vortex sensor $\Theta$ by Ducros et al.[10]

$$\Theta = \frac{(\nabla \cdot \mathbf{u})^2}{(\nabla \cdot \mathbf{u})^2 + |\nabla \times \mathbf{u}|^2}. \tag{34}$$

A spectral analysis on the utilization of $\Theta$ is given in the work of Pont et al.[3]

## III. Numerical Experiments

The accuracy of the proposed scheme is presented for three numerical testcases. The error is analyzed with the $L_2$-norm $E_{L_2(\Omega)}$

$$E_{L_2(\Omega)} = \left[ \frac{\sum_{\alpha=1}^{N} \left( \overline{\phi}_\alpha - \overline{\phi}_\alpha^{\text{ex}} \right)^2 |\Omega_\alpha|}{\sum_{\alpha=1}^{N} |\Omega_\alpha|} \right]^{1/2}, \tag{35}$$

with the volume-averaged, exact solution $\overline{\phi}_\alpha^{\text{ex}}$ and the total number of cells $N$. In order to examine the influence of mesh distortions on the numerical error, the benchmark tests are performed on two different grid types, shown in Figure 2. Besides the 2-exact reconstruction scheme, simulations are carried out using a 1-exact reconstruction approach, as well as a conventional central differencing scheme, referred to as 0-exact central scheme. To approximate the face fluxes, the 1-exact scheme utilizes reconstruction polynomials according to equation (10) as well as the 1-exact gradient operator (19). For the 0-exact scheme, no gradient correction is employed and face fluxes are approximated through volume-averages of adjacent cells with a central differencing approach. This scheme yields a spatial error of $\mathcal{O}(h^2)$ on regular, cartesian grids, but produces an error of $\mathcal{O}(0)$ if the mesh is distorted.

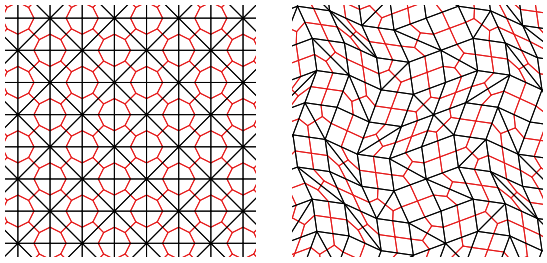

(a) Cartesian triangles (b) Deformed mixed

Figure 2: Grids for the accuracy benchmarks. Primary grid $\mathcal{P}(\Omega)$ connectivites are depicted in black and the respective median dual grid tessellation $\mathcal{D}(\Omega)$ in red.

### A. Scalar Gradient Testcase

To show the influence of the correction matrices $\mathbf{G}_\alpha$, $\mathbf{H}_\alpha$ and $\mathbf{G}_\alpha^*$, the gradient of a scalar function $\phi(\mathbf{x})$ is approximated by means of different gradient operators on a periodic domain $\mathbf{x} \in [0, 10L]^2$ with a unit length $L$. The scalar function $\phi(\mathbf{x})$ is defined by

$$\phi(\mathbf{x}) = A \left[ \cos(8\pi(x_1 - x_{1,0})) + \cos(8\pi(x_2 - x_{2,0})) \right] e^{-\frac{(x_1 - x_{1,0})^2 + (x_2 - x_{2,0})^2}{\sigma^2}}, \tag{36}$$

with $\mathbf{x}_0 = [5L, 5L]^T$, $A = 10$, $\sigma = \sqrt{3/2}L$. The analytical solution is shown in Figure 3a. The domain is discretized through a mesh consisting of deformed mixed elements and with mean cell widths varying from $L/4$ to $L/100$. Figure 3b shows calculated $L_2$-errors for all three gradient operator types. The 0-exact gradient operator is limited by an error bound, showing the $\mathcal{O}(1)$ accuracy limitation due to the highly distorted elements. In contrast, the one- and two-fold correction of the gradient operator leads to the specified error orders $\mathcal{O}(h)$ and $\mathcal{O}(h^2)$.

### B. Linear Convection Testcase

In this testcase, a scalar quantity is convected on a uniform flow field $\mathbf{u} = [1, 0]^T$ in a periodic domain $\mathbf{x} \in [0, 10L]^2$ with a unit length $L$. Equation (1) is discretized with a Crank-Nicolson scheme in time and the source term $S$ is neglected:

$$\frac{\phi^{n+1} - \phi^n}{\Delta t} + \frac{1}{2} \nabla \cdot (\mathbf{u}\phi)^{n+1} + \frac{1}{2} \nabla \cdot (\mathbf{u}\phi)^n = 0. \tag{37}$$

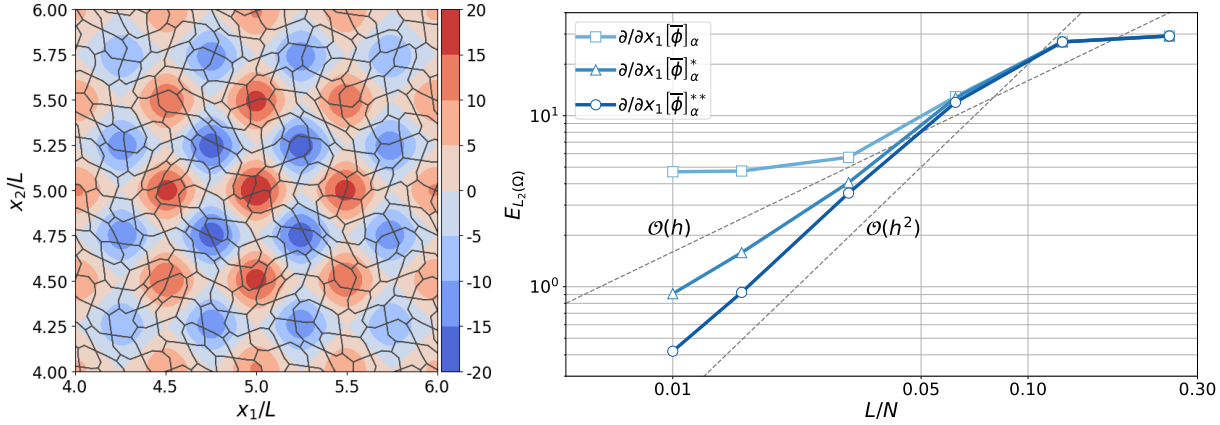


(a) Gradient test function $\phi(\mathbf{x})$ and median dual grid tesselation $\mathcal{D}(\Omega)$ for $L/40$

(b) Calculated $L_2$-error for the scalar gradient benchmark test.

Figure 3: Influence of the gradient operator type on the $L_2$-error for deformed mixed element grids.

A Gaussian pulse function is employed as initial distribution for the convected scalar $\phi$

$$\phi(\mathbf{x}, t = 0) = A\, e^{-\frac{(x-x_0)^2+(y-y_0)^2}{\sigma^2}}, \tag{38}$$

with $\mathbf{x}_0 = [5L, 5L]^T$, $A = 0.8$ and $\sigma = L/\sqrt{2\ln(2)}$. The scalar function is convected through the domain for a distance of $10L$ with mean cell widths varying from $L/4$ to $L/32$. A CFL number of 0.01 is employed for all simulations, in order to reduce the influence of temporal discretization errors.

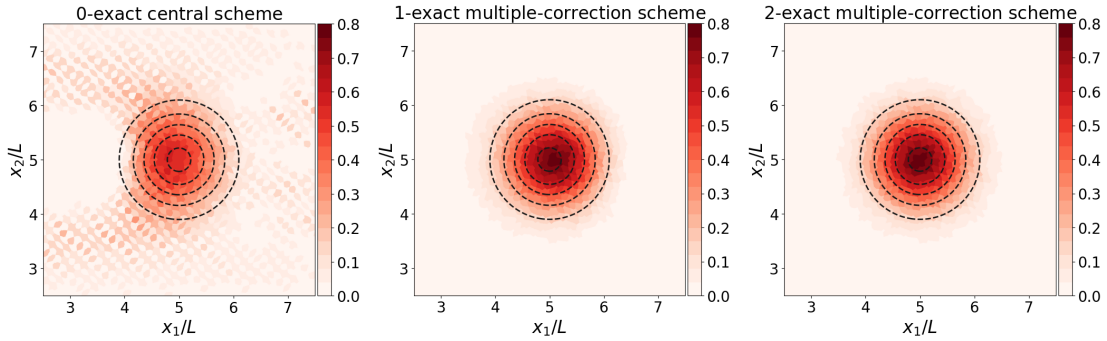


Figure 4: Volume-averages $\overline{\phi}_\alpha$ after the convection of $10L$ on deformed mixed primary grid elements with a grid resolution of $L/8$. The analytical solution is indicated in black dashed lines.

Figure 4 shows the solution after a convection distance of $10L$ on a mesh with deformed mixed elements and a resolution of $L/8$. The solution of the 0-exact central scheme is highly distorted, whereas both 1- and 2-exact reconstruction schemes feature low dissipative and dispersive errors. The calculated values for $E_{L_2(\Omega)}$ for both grids are provided in Figure 5. Respective mean iteration times for one single timestep on the cartesian triangular grid are given in Table 2. For this grid type, the truncation errors of all three schemes fall with prescribed orders of accuracy. The 2-exact reconstruction performs remarkably better than both other approaches, although it requires about two to three times the computation time compared to the conventional 0-exact central scheme. However, the 2-exact scheme already undercuts an error threshold of $E_{L_2(\Omega)} \leq 10^{-3}$ for a cell width of $L/8$, whereas the 0-exact scheme requires a resolution of $L/32$. Comparing the mean iteration times once again, the 2-exact scheme requires roughly 12% of the computation time of the 0-exact scheme, since 94% of the cells can be saved. For the mixed grid, the error of the 0-exact central scheme remains high due to the highly deformed elements. Both multiple-correction schemes produce similar numerical errors on mixed elements compared to the triangular mesh type, with a marginal reduction in the order of accuracy for the 2-exact scheme.

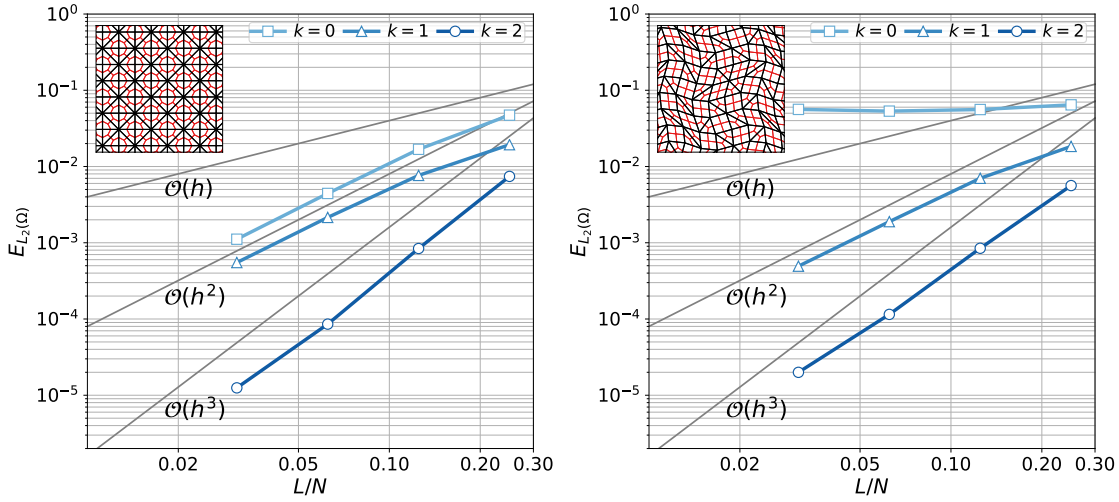


(a) Cartesian triangular elements

(b) Deformed mixed elements

Figure 5: $L_2$-Error norms of $\phi(\mathbf{x})$ for different meshes with varying discretization widths $L/N$. The exactness of the reconstruction polynomial is given by the value of $k$.

Table 1: Mean computation time for a single timestep in milliseconds for the linear convection testcase on cartesian triangular grids.

| Exactness $k$ | $L/4$ | $L/8$ | $L/16$ | $L/32$ |
|---|---|---|---|---|
| 0 | 21.80 | 63.11 | 315.31 | 1720.41 |
| 1 | 20.33 | 89.88 | 446.72 | 2074.15 |
| 2 | 41.65 | 207.84 | 1116.83 | 3132.40 |

### C. Vortex Convection Testcase

Finally, the schemes are tested on their performace for the nonlinear convection of a scalar quantity, by solving the incompressible Euler equations:

$$\nabla \cdot \mathbf{u} = 0, \tag{39}$$

$$\frac{\partial \mathbf{u}}{\partial t} + \nabla \cdot (\mathbf{u} \otimes \mathbf{u}) = -\frac{1}{\rho} \nabla p. \tag{40}$$

The coupling between pressure and velocity is realized using a projection method.[11] An interim velocity-field $\mathbf{u}^*$, which does not satisfy continuity, is predicted from the pressure field at the initial timestep $n$. The Crank-Nicolson scheme is employed for the temporal discretization of the predictor step:

$$\frac{\mathbf{u}^* - \mathbf{u}^n}{\Delta t} + \frac{1}{2} \nabla \cdot (\mathbf{u}^n \otimes \mathbf{u}^*) + \frac{1}{2} \nabla \cdot (\mathbf{u}^n \otimes \mathbf{u}^n) = -\frac{1}{\rho} \nabla p^n. \tag{41}$$

The pressure-field at the new timestep $n+1$ is obtained by the solution of a Poisson equation

$$\nabla \cdot (\nabla \delta p) = \frac{\rho}{\Delta t} \nabla \cdot \mathbf{u}^*, \tag{42}$$

with $\delta p = p^{n+1} - p^n$. Since a collocated arrangement of pressure and velocity is employed, a Rhie-Chow stabilization term[12] is added to the right-hand side of equation (42), preventing odd-even decoupling. This term introduces a spatial error of $\mathcal{O}(h^3)$.[13] The estimated pressure is used to obtain a divergence-free velocity-field at timestep $n+1$:

$$\mathbf{u}^{n+1} = \mathbf{u}^* - \frac{\Delta t}{\rho} \nabla p^{n+1}. \tag{43}$$

The divergence operators $\nabla \cdot (\dots)$ in equations (41) and (42) are discretized similarly to the convective divergence operator (1), employing the multiple-correction approach. A matrix free, biconjugate gradient stabilized method[14] is used for solving the linear system of equations. The numerical accuracy is tested through a vortex transport in a periodic domain $\mathbf{x} \in [0, 20L]^2$ with freestream conditions $u_\infty$, $p_\infty$ and a convection distance of $60L$. The initial conditions for velocity $\mathbf{u} = (u, v)$ and pressure $p$ are

$$u(\mathbf{x}, t=0) = u_\infty - \frac{\Gamma\,(y - y_0)}{\sigma} e^{-\frac{(x-x_0)^2+(y-y_0)^2}{2\sigma^2}}, \tag{44a}$$

$$v(\mathbf{x}, t=0) = \frac{\Gamma\,(x - x_0)}{\sigma} e^{-\frac{(x-x_0)^2+(y-y_0)^2}{2\sigma^2}}, \tag{44b}$$

$$p(\mathbf{x}, t=0) = p_\infty - \frac{1}{2}\rho\left(\frac{\Gamma}{\sigma}\right)^2 e^{-\frac{(x-x_0)^2+(y-y_0)^2}{\sigma^2}}, \tag{44c}$$

with $\sigma = L/\sqrt{2\ln(2)}$, $\Gamma/u_\infty = 0.8$ and $\mathbf{x}_0 = (10L, 10L)$. Additionally, equation (37) is solved for a scalar field variable $\phi$, with the same initial conditions as defined in equation (38). Since $\phi(\mathbf{x}, t=0)$ has the same radial extent as the vortex, its shape must be preserved during the convection process and can thus be used to evaluate the solution. Simulations are carried out on grids with resolutions ranging from $L/2$ to $L/16$.

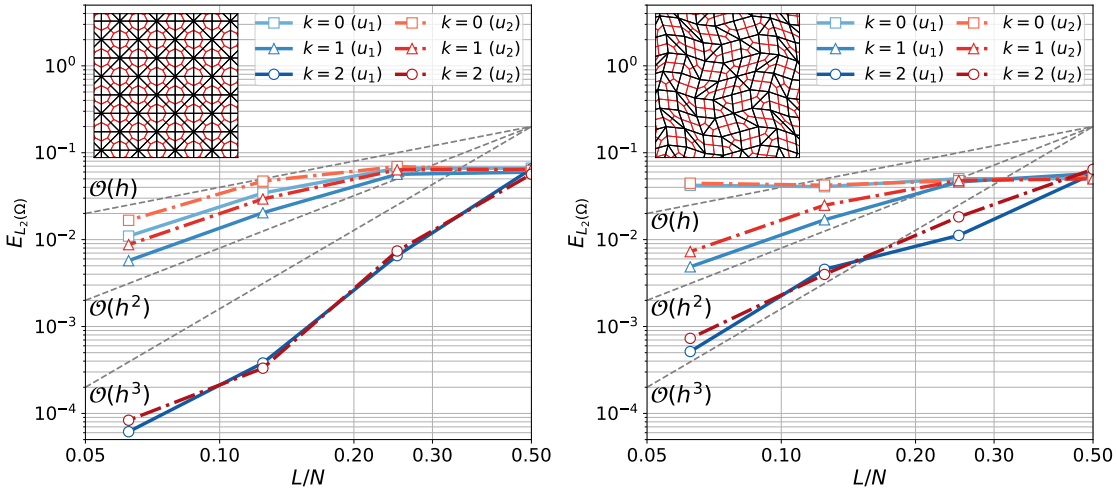


(a) Cartesian triangular elements

(b) Deformed mixed elements

Figure 6: $L_2$-Error norms of the velocity components $u_1$ and $u_2$ for different meshes with varying mesh resolution $L/N$.

The $L_2$-errors for the velocity components $u_1$ and $u_2$, pressure $p$ and the scalar field variable $\phi$ are shown in Figures 6 and 7. The 2-exact reconstruction approach offers the lowest $L_2$-errors for all variables, followed by the 1-exact scheme and the central scheme. Slight differences are present in the error curves of the velocitites $u_1$ and $u_2$, since the vortex is convected in the $x_1$-direction of the domain. For the triangular mesh type, the three schemes fall in their prescribed numerical orders, except the pressure for the 2-exact reconstruction, which changes into a second order for $L/8$. This also influences the errors of the velocity components $u_1$ and $u_2$. This is due to the fact, that the face values $(\nabla\delta p)_\Gamma$ on the discretized left hand side of equation (42) are approximated through equation (31), which rises with $\mathcal{O}(h^2)$. However, comparing Figures 6a and 6b, it seems that this error comes into effect for errors $E_{L_2(\Omega)} \leq 10^{-4}$. Compared to the triangular meshes, the solution from the mixed element grids shows larger numerical inaccuracies for the 2-exact reconstruction scheme. This can be explained by the fact, that median dual cells composed of only triangular primary grid elements are connected to more neighbors than in the mixed element case, leading to a higher accuracy and a more robust reconstruction. This also supports the assumption, that the vertex-centered multiple-correction approach lowers numerical errors in contrast to the cell-centered approach. Like for the linear convection testcase, a grid refinement does not lead to an enhanced solution for the 0-exact central scheme, when calculated on the mixed element grid.

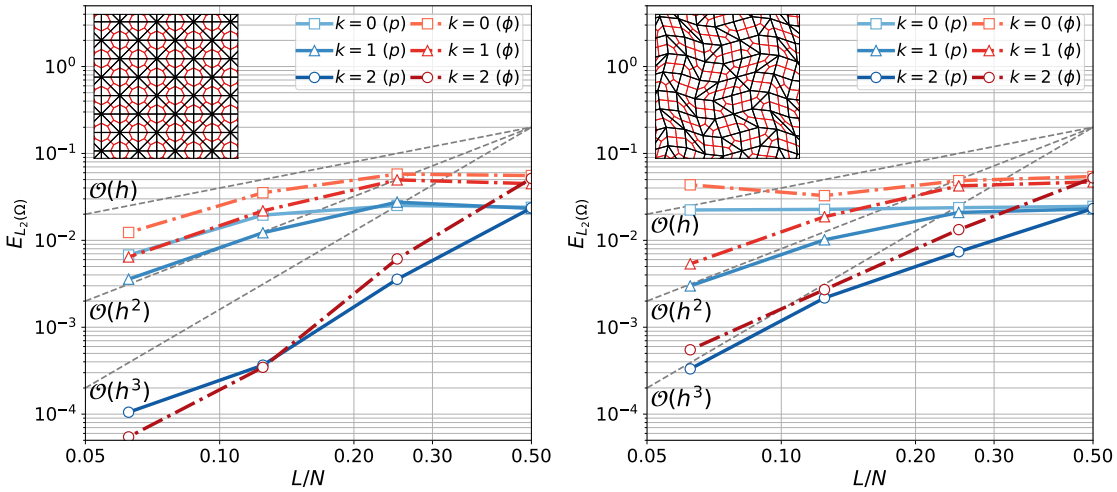


(a) Cartesian triangles

(b) Deformed mixed

Figure 7: $L_2$-Error norms of the pressure $p$ and the scalar field variable $\phi$ for different meshes with varying mesh resolution $L/N$.

Table 2: Mean computation time for a single timestep in milliseconds for the Euler vortex convection testcase on cartesian triangular grids.

| Exactness $k$ | $L/2$ | $L/4$ | $L/8$ | $L/16$ |
|---|---|---|---|---|
| 0 | 30.61 | 108.42 | 419.34 | 1619.04 |
| 1 | 45.47 | 160.42 | 547.66 | 1925.67 |
| 2 | 111.34 | 310.16 | 1127.87 | 3605.91 |

Figure 8 shows the solution of $\overline{u}_1$ after a convection distance of $60L$ on both grid types with resolutions $L/4$ and $L/16$. The dispersion properties of the schemes can be observed by comparing the solution of $\overline{u}_1$ to the analytical vortex shape, indicated in black. The 0-exact central scheme shows high deviations in the vortex position towards the analytical solution, when the triangular mesh with a cell width of $L/4$ is employed. This dispersive error is significantly reduced if the 1-exact scheme is used and almost vanishes for the 2-exact reconstruction approach. The solutions obtained with both 1- and 2-exact schemes are almost independent of the employed grid elements, whereas the quality of the solution obtained with the conventional central scheme strongly deviates when the mesh with mixed primary grid elements is employed. Even for the highly resolved mesh with a cell width of $L/16$, the solution obtained from the conventional central scheme shows large discrepancies to the analytical solution. Table 2 shows mean computation times for a single timestep on the cartesian triangular mesh. Similar to the linear convection testcase, the mean computation time for a single timestep of the 2-exact scheme is about two to three times as high as for the 0-exact central scheme. Nevertheless, the 2-exact scheme achieves an error of $E_{L_2(\Omega)} \leq 10^{-2}$ with a resolution of $L/4$, whereas both the 0-exact and 1-exact scheme require a mean cell width of $L/16$. This becomes clear in the comparison of Figures 8a and 8b, where the calculated solution of the 2-exact scheme clearly preserves the vortex shape and position on the coarse grid with only minor displacements, whereas both the 0-exact central scheme and the 1-exact multiple-correction scheme require a considerably higher amount of cells. For this reason it can be stated that the 2-exact scheme requires only 19% of the computation time to calculate a solution of equivalent quality for this testcase. Compared to the 0-exact central scheme, again roughly 93% of the elements can be saved. This can also be seen for the grid with skewed mixed elements.

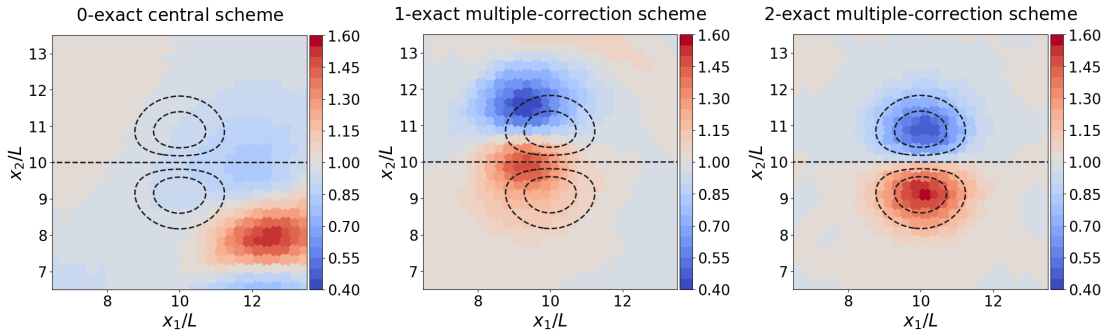


(a) Cartesian triangular elements with grid resolution $L/4$

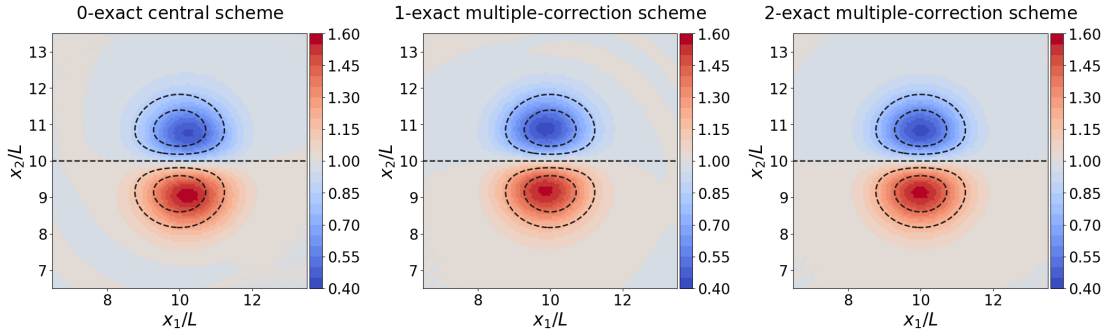


(b) Cartesian triangular elements with grid resolution $L/16$

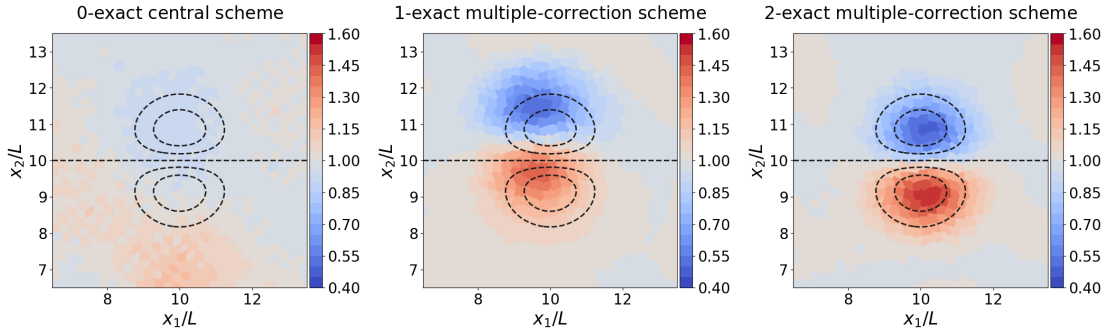


(c) Skewed mixed elements with grid resolution $L/4$

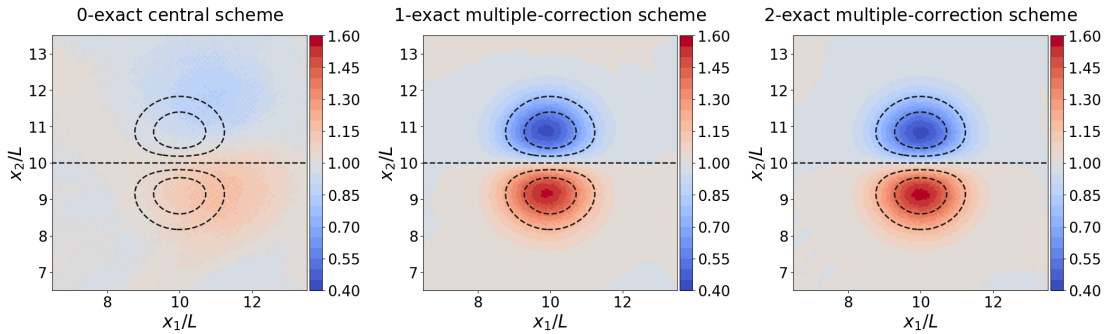


(d) Skewed mixed elements with grid resolution $L/16$

Figure 8: Volume-averages $\overline{u}_{1,\alpha}$ after the convection of $60L$ on both grid types with different resolutions. The analytical solution is indicated in black dashed lines.

## IV. Conclusion

A new discretization scheme based on the multiple-correction hybrid $k$-exact scheme by Pont et al.[3] has been proposed. The original approach, derived for the cell-centered finite volume method, was extended for vertex-centered grids in this work. A 2-exact reconstruction is established in the vicinity of a median dual cell by relating approximate derivatives to the reconstruction polynomial coefficients. The truncation error of the derivatives is successively reduced through grid dependent correction matrices, leading to an overall third-order accuracy for the spatial discretization of the convective operator. The capabilities of the scheme have been demonstrated on various numerical testcases and were compared to a 1-exact discretization and a conventional 0-exact central scheme. The influence of the correction matrices on the gradient operator and a third-order accuracy for the convective operator on strongly deformed grids were shown. Finally, the incompressible Euler equations were discretized with a projection method approach, in order to test the scheme for the nonlinear vortex convection testcase. In this context, the applicability of the proposed approach for the elliptic Poisson's equation was shown, which must be solved for the pressure-velocity coupling. The vortex structure could be resolved well, even for highly skewed meshes consisting of mixed triangular/quadrilateral elements. Compared to the conventional method, the proposed scheme requires about two to three times more computing time for the same number of elements. However, a similar quality of the solution can be achieved with a considerable reduction in the number of elements. This ultimately leads to a significant reduction in computing time for a desired level of accuracy. For future work, it remains to demonstrate the potential of the scheme for three dimensional, fully turbulent flows.

## References


[1]Ekaterinaris, J. A., "High-Order Accurate, Low Numerical Diffusion Methods for Aerodynamics," *Progress in Aerospace Sciences*, Vol. 41, No. 3-4, 2005, pp. 192–300.

[2]Barth, T. and Frederickson, P., "Higher Order Solution of the Euler Equations on Unstructured Grids using Quadratic Reconstruction," *28th Aerospace Sciences Meeting*, 1990, p. 13.

[3]Pont, G., Brenner, P., Cinnella, P., Maugars, B., and Robinet, J.-C., "Multiple-correction hybrid k-exact schemes for high-order compressible RANS-LES simulations on fully unstructured grids," *Journal of Computational Physics*, Vol. 350, 2017, pp. 45–83.

[4]Haider, F., Bertier, N., Courbet, B., Vuillot, F., and Croisille, J., "Application of a High Order Finite Volume Scheme on Unstructured Grids to Fluid Dynamics and Aerothermochemistry," hal-01111360.

[5]Haider, F., Brenner, P., Courbet, B., and Croisille, J. P., "Efficient Implementation of High Order Reconstruction in Finite Volume Methods," *Finite Volumes for Complex Applications VI - Problems and Perspectives, Springer Proceedings in Mathematics*, Vol. 4, 2011, pp. 553–560.

[6]Haider, F., *Discrétisation en maillage non structuré général et applications LES*, Ph.D. thesis, Université Pierre et Marie Curie-Paris VI, 2009.

[7]Charest, M. R., Canfield, T. R., Morgan, N. R., Waltz, J., and Wohlbier, J. G., "A High-Order Vertex-Based Central ENO Finite-Volume Scheme for Three-Dimensional Compressible Flows," *Computers & Fluids*, Vol. 114, 2015, pp. 172–192.

[8]Ollivier-Gooch, C. and Van Altena, M., "A High-Order-Accurate Unstructured Mesh Finite-Volume Scheme for the Advection-Diffusion Equation," *Journal of Computational Physics*, Vol. 181, No. 2, 2002, pp. 729–752.

[9]Pozo, J. M., Villa-Uriol, M.-C., and Frangi, A. F., "Efficient 3D Geometric and Zernike Moments Computation from Unstructured Surface Meshes," *IEEE Transactions on Pattern Analysis and Machine Intelligence*, Vol. 33, No. 3, 2011, pp. 471–484.

[10]Ducros, F., Ferrand, V., Nicoud, F., Weber, C., Darracq, D., Gacherieu, C., and Poinsot, T., "Large-Eddy Simulation of the Shock/Turbulence Interaction," *Journal of Computational Physics*, Vol. 152, No. 2, 1999, pp. 517–549.

[11]Chorin, A. J., "A Numerical Method for Solving Incompressible Viscous Flow Problems," *Journal of Computational Physics*, Vol. 2, No. 1, 1967, pp. 12–26.

[12]Rhie, C. and Chow, W. L., "Numerical Study of the Turbulent Flow Past an Airfoil with Trailing Edge Separation," *AIAA journal*, Vol. 21, No. 11, 1983, pp. 1525–1532.

[13]Versteeg, H. K. and Malalasekera, W., *An Introduction to Computational Fluid Dynamics: The Finite Volume Method*, Pearson Education, 2007.

[14]Van der Vorst, H. A., "Bi-CGSTAB: A fast and Smoothly Converging Variant of Bi-CG for the Solution of Nonsymmetric Linear Systems," *SIAM Journal on Scientific and Statistical Computing*, Vol. 13, No. 2, 1992, pp. 631–644.

## A. On the Derivation of the 2-Exact Hessian Correction Matrix

Starting point for the derivation of the correction matrix for the 2-exact Hessian operator of a cell $\Omega_\alpha$ is the 1-exact gradient operator for a median dual cell $\Omega_\beta$ in the first neighborhood of $\Omega_\alpha$.

$$\frac{\partial}{\partial x_i}\big[\,\overline{\phi}\,\big]^*_\beta = \frac{G^{-1}_{ij,\beta}}{|\Omega_\beta|}\sum_{\gamma\in\mathbb{V}^{(1)}_\beta}\left[w_{\beta\gamma}\overline{\phi}_\gamma + (1-w_{\beta\gamma})\,\overline{\phi}_\beta\right]\mathcal{S}^{(\beta\gamma)}_j. \tag{45}$$

Similar to the derivation of the 1-exact gradient operator, the value of $\overline{\phi}_\gamma$ is approximated by integrating the 2-exact reconstruction function (7) over $\Omega_\beta$.

$$\overline{\phi}_\gamma = \overline{\phi}_\beta + \left.\frac{\partial\phi}{\partial x_i}\right|_{\mathbf{x}_\beta}\left(\mathcal{M}^{(\gamma,\beta)}_i - \mathcal{M}^{(\beta,\beta)}_i\right) + \frac{1}{2}\left.\frac{\partial^2\phi}{\partial x_j\partial x_k}\right|_{\mathbf{x}_\beta}\left(\mathcal{M}^{(\gamma,\beta)}_{jk} - \mathcal{M}^{(\beta,\beta)}_{jk}\right) + \mathcal{O}(h^3). \tag{46}$$

Inserting equation (46) into (45) leads to the following formulation:

$$\begin{aligned}\frac{\partial}{\partial x_i}\big[\,\overline{\phi}\,\big]^*_\beta = {} & \overbrace{\frac{G^{-1}_{ij,\beta}}{|\Omega_\beta|}\sum_{\gamma\in\mathbb{V}^{(1)}_\beta} w_{\beta\gamma}\left[\left.\frac{\partial\phi}{\partial x_k}\right|_{\mathbf{x}_\beta}\left(\mathcal{M}^{(\gamma,\beta)}_k - \mathcal{M}^{(\beta,\beta)}_k\right)\right]\mathcal{S}^{(\beta\gamma)}_j}^{=\left.\frac{\partial\phi}{\partial x_i}\right|_{\mathbf{x}_\beta}} \\ & + \frac{1}{2}\frac{G^{-1}_{ij,\beta}}{|\Omega_\beta|}\sum_{\gamma\in\mathbb{V}^{(1)}_\beta} w_{\beta\gamma}\left[\left.\frac{\partial^2\phi}{\partial x_l\partial x_m}\right|_{\mathbf{x}_\beta}\left(\mathcal{M}^{(\gamma,\beta)}_{lm} - \mathcal{M}^{(\beta,\beta)}_{lm}\right)\right]\mathcal{S}^{(\beta\gamma)}_j \\ & + \underbrace{\frac{G^{-1}_{ij,\beta}}{|\Omega_\beta|}\overline{\phi}_\beta\sum_{\gamma\in\mathbb{V}^{(1)}_\beta}\mathcal{S}^{(\beta\gamma)}_j}_{=0}.\end{aligned} \tag{47}$$

The first term on the right-hand side of equation (47) can be simplified to $\left.\frac{\partial\phi}{\partial x_i}\right|_{\mathbf{x}_\beta}$, due to the definition of matrix $\mathbf{G}_\beta$. Because of geometric conservation, the last term cancels out. The second term can be simplified by introducing the 1-exact gradient of the rank 2 geometric volume moment

$$\frac{\partial}{\partial x_i}\big[\,\mathcal{M}_{kl}\,\big]^*_\beta = \frac{G^{-1}_{ij,\beta}}{|\Omega_\beta|}\sum_{\gamma\in\mathbb{V}^{(1)}_\beta}\left[w_{\beta\gamma}\mathcal{M}^{(\gamma,\beta)}_{kl} + (1-w_{\beta\gamma})\,\mathcal{M}^{(\beta,\beta)}_{kl}\right]\mathcal{S}^{(\beta\gamma)}_j. \tag{48}$$

Finally, the 1-exact gradient on $\Omega_\beta$ can be expressed through the relation

$$\frac{\partial}{\partial x_i}\big[\,\overline{\phi}\,\big]^*_\beta = \left.\frac{\partial\phi}{\partial x_i}\right|_{\mathbf{x}_\beta} + \frac{1}{2}\left.\frac{\partial^2\phi}{\partial x_j\partial x_k}\right|_{\mathbf{x}_\beta}\frac{\partial}{\partial x_i}\big[\,\mathcal{M}_{jk}\,\big]^*_\beta + \mathcal{O}(h^2). \tag{49}$$

Next, the reconstruction polynomial is considered on cell $\Omega_\alpha$. Differentiation of equation (7) leads to the following relations between the adjacent cells $\Omega_\alpha$ and $\Omega_\beta$

$$\left.\frac{\partial\phi}{\partial x_i}\right|_{\mathbf{x}_\beta} = \left.\frac{\partial\phi}{\partial x_i}\right|_{\mathbf{x}_\alpha} + \left.\frac{\partial^2\phi}{\partial x_i\partial x_j}\right|_{\mathbf{x}_\alpha}(x_{j,\beta} - x_{j,\alpha}) + \mathcal{O}(h^2), \tag{50a}$$

$$\left.\frac{\partial^2\phi}{\partial x_i\partial x_j}\right|_{\mathbf{x}_\beta} = \left.\frac{\partial^2\phi}{\partial x_i\partial x_j}\right|_{\mathbf{x}_\alpha} + \mathcal{O}(h). \tag{50b}$$

These definitions are utilized to express the 1-exact gradient of $\frac{\partial}{\partial x_i}\big[\,\overline{\phi}\,\big]^*_\beta$ in terms of derivatives of $\Omega_\alpha$

$$\frac{\partial}{\partial x_i}\big[\,\overline{\phi}\,\big]^*_\beta = \left.\frac{\partial\phi}{\partial x_i}\right|_{\mathbf{x}_\alpha} + \left.\frac{\partial^2\phi}{\partial x_i\partial x_j}\right|_{\mathbf{x}_\alpha}(x_{j,\beta} - x_{j,\alpha}) + \frac{1}{2}\left.\frac{\partial^2\phi}{\partial x_k\partial x_l}\right|_{\mathbf{x}_\alpha}\frac{\partial}{\partial x_i}\big[\,\mathcal{M}_{kl}\,\big]^*_\beta. \tag{51}$$

The relation for $\frac{\partial}{\partial x_i}\left[\,\overline{\phi}\,\right]^*_\beta$ is inserted into the 0-exact Hessian matrix operator $\frac{\partial^2}{\partial x_i \partial x_j}\left[\,\overline{\phi}\,\right]_\alpha$ in equation (20). Expanding this expression and cancelling terms, results in

$$\begin{aligned}\frac{\partial^2}{\partial x_i \partial x_j}\left[\,\overline{\phi}\,\right]_\alpha = &\overbrace{\left[\frac{1}{|\Omega_\alpha|}\sum_{\beta\in\mathbb{V}^{(1)}_\alpha} w_{\alpha\beta}\left(x_{k,\beta}-x_{k,\alpha}\right)\mathcal{S}_i^{(\alpha\beta)}\right]}^{=\frac{\partial}{\partial x_i}\left[\,x_k\,\right]_\alpha}\left.\frac{\partial^2\phi}{\partial x_j\partial x_k}\right|_{\mathbf{x}_\alpha}\\ &+\frac{1}{2}\underbrace{\left[\frac{1}{|\Omega_\alpha|}\sum_{\beta\in\mathbb{V}^{(1)}_\alpha} w_{\alpha\beta}\left(\frac{\partial}{\partial x_j}\left[\,\mathcal{M}_{lm}\,\right]^*_\beta-\frac{\partial}{\partial x_j}\left[\,\mathcal{M}_{lm}\,\right]^*_\alpha\right)\mathcal{S}_i^{(\alpha\beta)}\right]}_{=\frac{\partial^2}{\partial x_i\partial x_j}\left[\,\mathcal{M}_{lm}\,\right]_\alpha}\left.\frac{\partial^2\phi}{\partial x_l\partial x_m}\right|_{\mathbf{x}_\alpha}.\end{aligned} \tag{52}$$

After exploiting symmetry properties of the Hessian matrix and the rank 2 volume moment tensors, a final expression can be deduced which relates the 0-exact Hessian matrix operator to the 1-exact second derivatives:

$$\begin{aligned}\frac{\partial^2}{\partial x_i \partial x_j}\left[\,\overline{\phi}\,\right]_\alpha+\frac{\partial^2}{\partial x_j \partial x_i}\left[\,\overline{\phi}\,\right]_\alpha = &\frac{\partial}{\partial x_i}\left[\,x_k\,\right]_\alpha\left.\frac{\partial^2\phi}{\partial x_j\partial x_k}\right|_{\mathbf{x}_\alpha}+\frac{1}{2}\frac{\partial^2}{\partial x_i\partial x_j}\left[\,\mathcal{M}_{mn}\,\right]_\alpha\left.\frac{\partial^2\phi}{\partial x_m\partial x_n}\right|_{\mathbf{x}_\alpha}\\ &+\frac{\partial}{\partial x_j}\left[\,x_l\,\right]_\alpha\left.\frac{\partial^2\phi}{\partial x_i\partial x_l}\right|_{\mathbf{x}_\alpha}+\frac{1}{2}\frac{\partial^2}{\partial x_j\partial x_i}\left[\,\mathcal{M}_{pq}\,\right]_\alpha\left.\frac{\partial^2\phi}{\partial x_p\partial x_q}\right|_{\mathbf{x}_\alpha}\\ &+\mathcal{O}(h).\end{aligned} \tag{53}$$

It can be shown, that the terms $\frac{\partial}{\partial x_i}\left[\,x_l\,\right]_\alpha$ equal the identity matrix $\delta_{il}$,[4] which finally leads to the expression in equation (21).